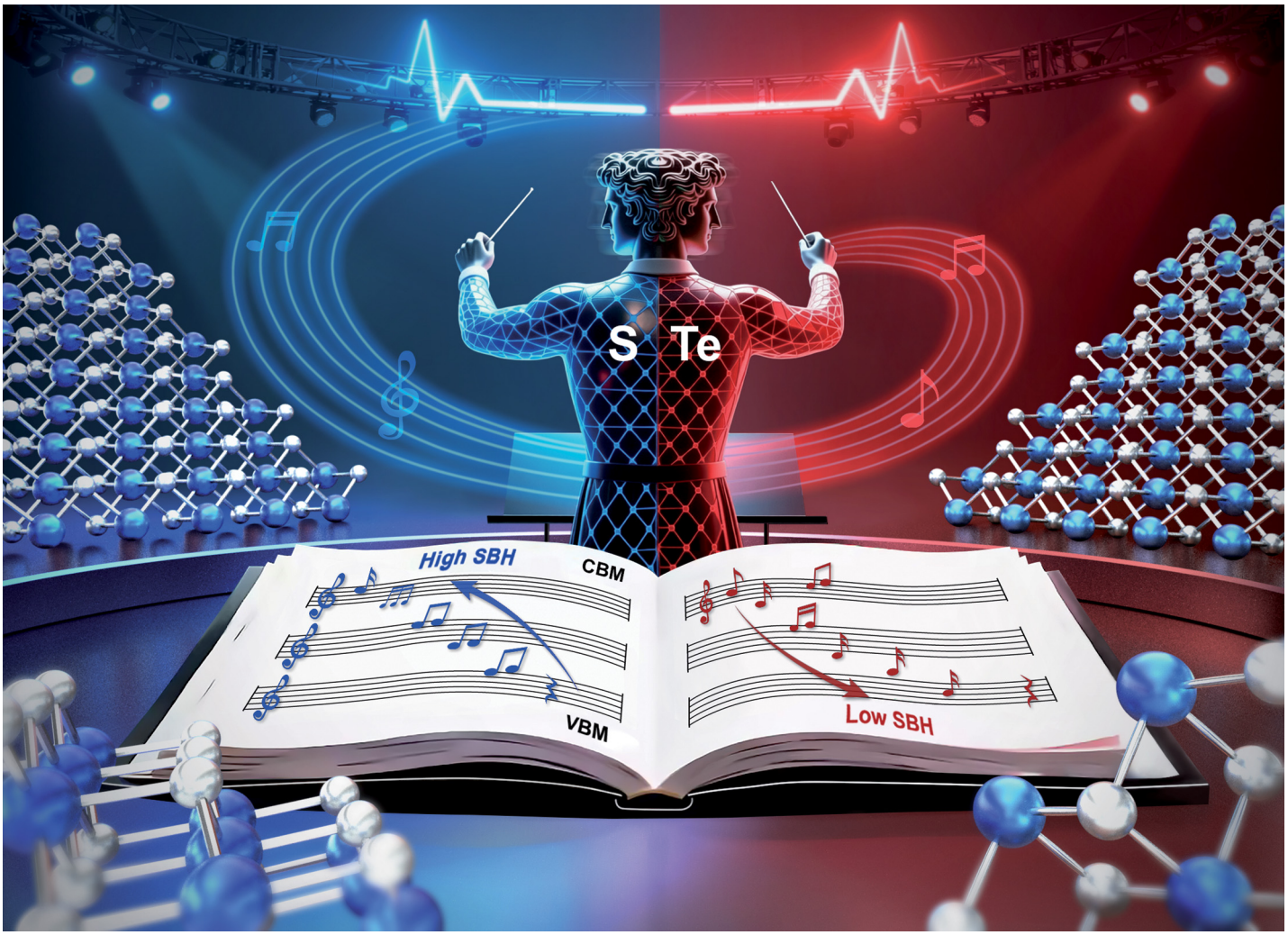

Showcasing research from Prof. Shaojuan Li's group at State Key Laboratory of Luminescence and Applications, Changchun Institute of Optics, Fine Mechanics and Physics, Chinese Academy of Sciences, Changchun, Jilin, China

Janus metal-enabled tunable Schottky barriers in van der Waals contacts *via* interfacial polarization modulations

We introduce a breakthrough strategy to overcome Fermi-level pinning using intrinsic polar Janus metals. By simply switching their contact surface (S- or Te-terminated), the Schottky barrier height and type can be effectively modulated *via* interfacial polarization, providing a general strategy toengineer metal–semiconductor interfaces.

Image reproduced by permission of Liujian Qi from *Mater. Horiz.*, 2025, **12**, 10630.

As featured in:

See Liujian Qi, Shaojuan Li *et al.*, *Mater. Horiz.*, 2025, **12**, 10630.

ROYAL SOCIETY OF CHEMISTRY

rsc.li/materials-horizons

Registered charity number: 207890

Materials Horizons

ROYAL SOCIETY OF CHEMISTRY

COMMUNICATION

View Article Online
View Journal | View Issue

Check for updates

Cite this: *Mater. Horiz.*, 2025, **12**, 10630

Received 13th August 2025,
Accepted 28th October 2025

DOI: 10.1039/d5mh01553g

rsc.li/materials-horizons

Janus metal-enabled tunable Schottky barriers in van der Waals contacts *via* interfacial polarization modulations

Yanze Feng,[ab] Liujian Qi,[*ab] Yu Du,[ab] Nan Zhang,[ab] Yuting Zou,[ab] Zhiming Shi,[ab] Dabing Li[ab] and Shaojuan Li[*ab]

Two-dimensional semiconductors exhibit exceptional potential in next-generation electronics; however, the strong Fermi-level pinning effect in the metal–semiconductor (M–S) contacts inevitably generates an unmodulated Schottky barrier, severely compromising device performance. Here, to address this challenge, we propose a novel strategy using the polar metallic Janus TaSTe originating from the broken structure symmetry. Specifically, by switching the S or Te surface in contact with a semiconductor, tunable M–S interface interactions have been effectively achieved by the Janus TaSTe electrode, which is determined by interfacial polarization due to the difference in the electronegativity of S and Te atoms. In addition, we show that under the external electric fields and strain, the heights and types of the Schottky barrier of Janus TaSTe–PtS_2 contact have been effectively tuned. We further demonstrate the universality of our strategy by expanding various M–S contacts between different Janus metals and semiconductors. Our results break through the limitation of work function and provide a novel way to tune the interfacial interactions between the metal and semiconductors, holding promising applications for future high-performance electronic devices.

New concepts

The effective manipulation of the Schottky barrier at the metal–semiconductor (M–S) contact remains a persistent challenge in the field of electronics due to the strong Fermi-level pinning effect. In this work, to solve this challenge, we propose a novel strategy by using polar metals originating from the asymmetric crystal structure and charge distributions. Diverging from prior studies limited to the dimension of singular work function due to the single interface contact governed by the out-of-plane symmetry of metal electrodes, our work introduces a polar metallic Janus TaSTe material as an electrode and achieves adjustable interface contacts with semiconductors benefitting from the broken out-of-plane mirror symmetry and polarization due to the electronegativity differences in S and Te elements, providing a distinct approach for modulating the Schottky barrier. By applying external electric fields and strain, the interfacial properties of the PtS_2–STaTe and PtS_2–TeTaS heterostructures can be effectively tuned, achieving the interconversion between n-type and p-type Schottky contacts. The universality of our results is further demonstrated by the effectively tunable Schottky barrier for various van der Waals Janus metal and semiconductor contacts. Our results elucidate the fundamental mechanisms governing M–S interface properties, offering significant potential for advancing high-performance electronic devices.

Introduction

Leveraging atomic-scale thickness, tunable bandgaps and weak interlayer coupling, two-dimensional van der Waals (vdW) materials exhibit unique electronic and optoelectronic properties, offering an unparalleled platform for the development of next-generation electronic devices.[1–5] The performance of electronic devices based on vdW materials is inevitably affected by the metal–semiconductor (M–S) interface quality, and a tunable interfacial contact barrier is crucial for designing and fabricating high-performance electronic devices.[6,7] In the case of conventional bulk metal and vdW semiconductor contacts, however, factors such as dangling bonds, imperfections, and lattice damage contribute to the strong Fermi-level pinning effect, which hinders the ability to tailor the barrier height by manipulating metal work functions and significantly impacts the electronic properties and charge transport capability of the devices.[8,9] Consequently, it is crucial to explore novel metal electrodes to advance the performance of the devices.

Recently, vdW M–S contacts have attracted growing interest as a promising strategy to mitigate the persistent challenge of the Fermi-level pinning effect in conventional M–S interfaces.[10–12] The weak interfacial interaction between vdW metals and semiconductors effectively prevents interfacial hybridization without dangling bonds or chemical disorders,

[a] State Key Laboratory of Luminescence Science and Technology, Changchun Institute of Optics, Fine Mechanics and Physics, Chinese Academy of Sciences, Changchun 130033, China. E-mail: qiliujian@ciomp.ac.cn, lishaojuan@ciomp.ac.cn
[b] University of Chinese Academy of Sciences (UCAS), Beijing 100049, China

giving rise to tunable contact barriers by changing the vdW metals with different work functions, which will effectively improve the overall performance of devices.[13–15] However, current research is predominantly restricted to vdW semimetals with out-of-plane mirror symmetric structures, which limits the ability to modulate M–S interface properties due to the singular interfacial contact.[16–18] In brief, current studies on the modulation of M–S contacts are solely limited to the dimension of singular work function, neglecting the effect of multi-faceted interfacial interactions. So far, the potential of the vdW metal with the intrinsically broken out-of-plane symmetry for achieving tunable vdW M–S interfaces remains rarely explored.

Polar metals, which exhibit the simultaneous coexistence of metallicity and polar structure, featuring intrinsic conduction and inversion symmetry breaking, have garnered significant attention due to their remarkable physical properties such as ferroelectricity and superconductivity.[19,20] Among polar metals, two dimensional vdW Janus structures have attracted increased level of interest due to the out-of-plane symmetry breaking.[21,22] Similar to the structure of Janus MoSSe and MoSH,[23,24] the non-centrosymmetric structure and different electronegativities of the two different elements on both sides of metallic Janus materials result in the asymmetric electron distribution and the overall out-of-plane polarization, which will enable the tunable interfacial coupling during the formation of heterostructures with semiconductors *via* the modulation of interfacial polarization. Therefore, it is expected that the formation of M–S contacts using Janus metals will effectively tune the Schottky barrier at the interface and break through the limited dimension of work function, providing a novel approach to regulate vdW M–S contact interfaces.

In this work, we go beyond the traditional and vdW metals and propose a novel strategy to achieve tunable Schottky barriers, by using the polar metals that originate from the asymmetric geometry structure and charge distribution. Based on first-principles calculations, we show that the interfacial properties such as Schottky barrier heights (SBHs) and types can be effectively modulated by the metallic polar Janus TaSTe with disparity in the electronegativity of S and Te elements on both sides of TaSTe. Additionally, the interconversion between n-type and p-type Schottky contacts for both PtS_2–STaTe and PtS_2–TeTaS interfaces can be effectively achieved by applying external electric fields and strain. Furthermore, the universality of our results has been demonstrated by the effectively regulatable Schottky barriers for various metallic Janus metal and semiconductor contacts. Our results transcend the limitation of the dimension of singular work function and provide a novel and universal strategy for tuning the interfacial properties of M–S contacts, showing significant promise for applications in high-performance electronic devices.

Computational methods

All theoretical calculations were performed using the Vienna *ab initio* simulation package (VASP) with the projector-augmented wave (PAW) method.[25,26] The Perdew–Burke–Ernzerhof (PBE) exchange–correlation functional and DFT-D3 vdW method were used for geometry optimizations.[27,28] The Heyd–Scuseria–Ernzerhof (HSE06) hybrid functional was employed to accurately calculate the electronic structures of all studied systems in this work.[29] A plane-wave energy cutoff of 500 eV and the fine *k*-sampling with a separation of 0.025 $Å^{-1}$ in the Brillouin zone were set for all calculations. The convergence criteria for the total energy and the maximal residual force were set to 1.0×10^{-5} eV and 0.01 eV $Å^{-1}$, respectively. A vacuum layer of 15 Å along the out-of-plane direction was set to prevent the interaction between the neighboring slabs. To evaluate the effect of lattice vibrations and thermal fluctuations on the interfacial charge redistribution of heterostructures, the *ab initio* molecular dynamics (AIMD) calculations were performed at 300 K using the Andersen thermostat and an NVT ensemble. The total time of AIMD was set to 10 ps with the time step of 1 fs.

When building the M–S heterostructures, different possible stacking structures were considered and the most stable structures were further considered, as shown in Fig. S1 and Table S1. Since the electronic properties of semiconductors play a crucial role in determining the device performance, we here focus on the electronic structures of semiconducting PtS_2, which is more sensitive to changes in lattice constants than metallic TaSTe. Therefore, to avoid the errors of the band structures of semiconductors induced by the external strain, the lattice constant of Janus metals was adjusted to match the lattice of semiconductors, and the corresponding lattice mismatches are shown in Table S2, with most of them being less than 4.2%. In addition, as shown in Fig. S2, we evaluated the electronic structures of metallic TaSTe under different strains studied in this work (0%, 1.7% and 4.2%) and found that both band structures and work functions of metallic TaSTe change slightly. Moreover, as shown in Table S3, taking PtS_2–ZrSTe and PtS_2–HfSTe systems as examples, we calculated the electronic properties of heterostructures with smaller lattice mismatches (1.37% and 0.32%, respectively; large periodic cells with 159 atoms) and found that SBHs slightly changed with the variation range of $\sim$0.1 eV compared with the case with large lattice mismatches (7.05% and 5.99%, respectively), which demonstrates the validity of our results.

Results and discussion

As a polar metal, TaSTe is a two-dimensional vdW material featuring a Janus structure analogous to the metallic MoSH (Fig. 1). It is noteworthy that the stability of Janus TaSTe has been confirmed by previous work.[30] Moreover, given that metallic Janus MoSH has already been synthesized experimentally from the precursor $MoSe_2$,[31] the structurally similar Janus TaSTe is likely synthesizable from its precursor TaS_2 or $TaSe_2$. As shown in Fig. 1a, to analyze the symmetry breaking nature of TaSTe, we calculated the charge density distribution and electron localization function. The larger electronegativity of the S element than Te element results in denser electron distributions

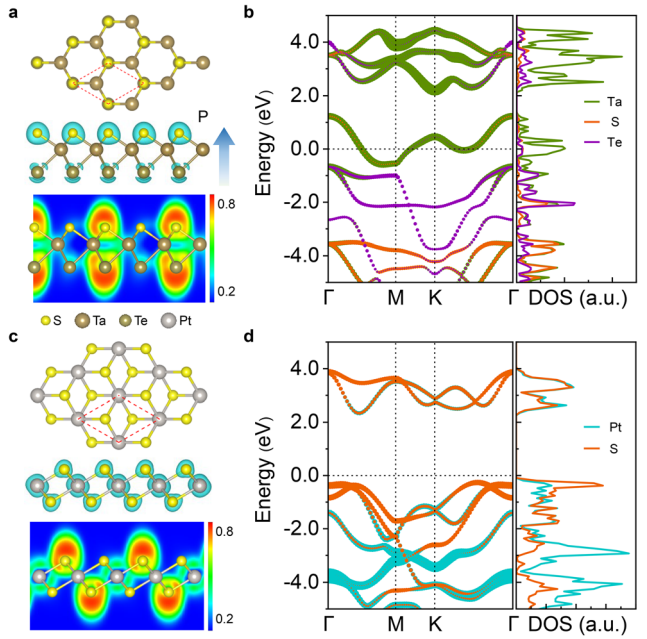

Fig. 1 (a) and (c) Lattice structures, charge density distributions and electron localization functions, (b) and (d) HSE band structures and density of states of monolayer TaSTe and monolayer PtS_2, respectively. The arrow in (a) indicates the out-of-plane polarization directed from the Te atom to the S atom. In both (a) and (c), the red dashed lines represent the unit cell, and the charge density isosurfaces are 0.08 and 0.15 e $Bohr^{-3}$, respectively.

around S atoms as well as the asymmetric distribution of the electron localization function along the out-of-plane direction, which leads to out-of-plane polarization. The calculated polarization of TaSTe is 0.19 Debye per unit cell (u.c.) along the orientation directed from the Te atom to S atom, which is comparable to that of other previously reported polar materials (for example, $CrSe_2$, 0.16 Debye per u.c.; VS_2, 0.48 Debye per u.c.).[32] We further calculated the band structure of TaSTe, which exhibits metallic behavior with the valence band mainly contributed by Ta orbitals crossing the Fermi level (Fig. 1b). For the vdW semiconductor, we chose PtS_2 as a prototype which has attracted growing attention in the field of electronics and optoelectronics.[33,34] Different from the polar structure of TaSTe, PtS_2 shows a higher symmetric structure, which can be seen from its symmetric electron distribution and electron localization function (Fig. 1c). In addition, the band structure of PtS_2 shows an indirect band gap of 2.59 eV with the conduction and valence bands contributed by both Pt and S orbitals (Fig. 1d), which is consistent with the previous results.[35,36]

Fig. 2 shows the interfacial properties of the PtS_2–TaSTe heterostructure. The Janus TaSTe with S and Te terminations on opposite surfaces enables two different types of vdW M–S contacts between TaSTe and PtS_2: interfacial contact between PtS_2 and the S termination (PtS_2–STaTe) and interfacial contact between PtS_2 and the Te termination (PtS_2–TeTaS), as shown in Fig. 2a and d. First, when the heterostructure interface is formed between PtS_2 and the S termination, there appears a distinct charge redistribution at the interface, as evidenced by the charge density difference depicted in Fig. 2b. Electron accumulation becomes prominent at the center of the interface, while electron depletion is localized at each side of the interface. We calculated the charge transfer in the interface and found the charge transfer of 3.4×10^{-4} e $Å^{-2}$ from PtS_2 to STaTe for PtS_2–STaTe systems, indicating the formation of interfacial polarization from PtS_2 to STaTe, which is opposite to the polarization of original STaTe. Our calculations show that the Schottky junction displays an overall polarization of 0.18 Debye per u.c. directed from the Te atom to S atom of TaSTe, validating the above polarisation calculations. Fig. 2c shows the projected band structure of the PtS_2–STaTe heterostructure, revealing the formation of an n-type Schottky contact. The n-type and p-type SBHs are defined as $\Phi_n = E_C - E_F$ and $\Phi_p = E_F - E_V$, where E_C, E_V, and E_F denote the energies of the conduction band minimum (CBM), valence band maximum (VBM), and Fermi level, respectively. More interestingly, the n-type SBH is almost equal to the p-type SBH, Φ_n = 1.26 eV and Φ_p = 1.28 eV, which suggests that the contact type transition can be readily modulated by external stimuli, such as electric field or strain.

Conversely, when the interfacial contact PtS_2–TeTaS is formed, the larger electronegativity of the S element in PtS_2 relative to the Te element in TaSTe induces pronounced electron accumulation near the PtS_2 side, with an obvious electron depletion region near the Te atoms side (Fig. 2e). The charge transfer is 3.3×10^{-3} e $Å^{-2}$ from TeTaS to PtS_2 for PtS_2–TeTaS systems, which is larger than that in PtS_2–STaTe heterostructure, indicating a larger interfacial polarization. The PtS_2–TeTaS Schottky junction displays an overall polarization of −0.10 Debye per u.c. directed from the Te atom to the S atom of TaSTe, validating the above polarisation calculations. Band structure analysis reveals a significantly lower SBH in PtS_2–TeTaS compared with the PtS_2–STaTe heterostructure (Φ_n = 0.97 eV and Φ_p = 0.92 eV), and the proximity SBH further indicates pronounced tunability between n-type and p-type Schottky contacts (Fig. 2f). To evaluate the effect of lattice vibrations and thermal fluctuations on the interfacial charge redistribution, we performed the AIMD calculations on the PtS_2–STaTe and PtS_2–TeTaS systems and found that the plane and three-dimensional charge density differences between the heterostructures at 0 K and 300 K remain nearly unchanged (Fig. S3), which indicates that the temperature has a mirror effect on the trend of the interfacial charge redistribution and validates the feasibility in practical applications.

We now study the tunability of the interfacial properties of PtS_2–TaSTe contacts. External electric fields and strain have been recognized as effective strategies for modulating the interactions at the M–S interface.[37,38] We first investigated the impact of external electric fields on the SBH of PtS_2–TaSTe contacts. As illustrated in Fig. 3a, linear relationships appear for both n-type and p-type SBHs of PtS_2–STaTe with the electric field strength when an electric field along the out-of-plane direction is applied to the M–S contact. Under a positive electric field, the n-type SBH gradually decreases while the p-type SBH increases, causing the M–S contact to exhibit n-type characteristics. Conversely, under a negative electric field, the p-type SBH

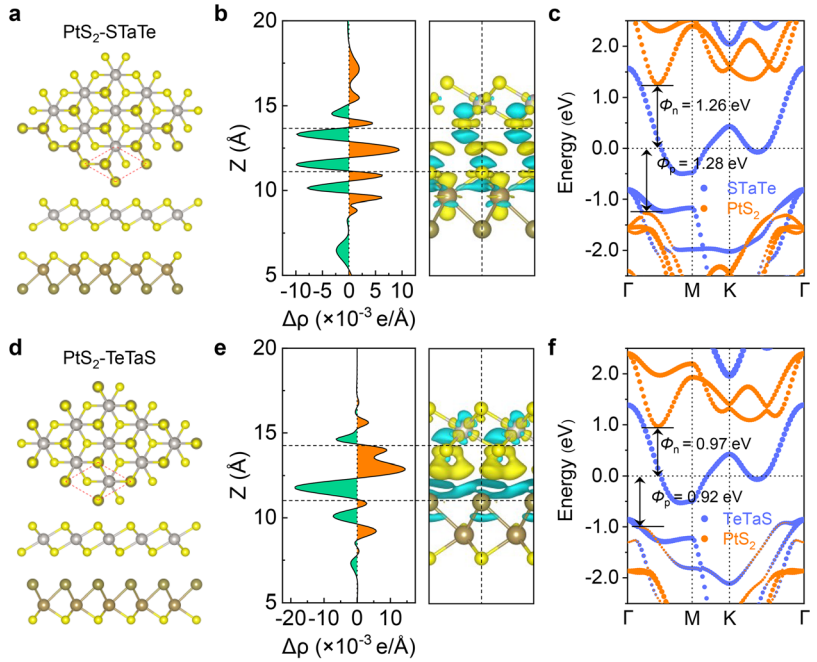

Fig. 2 (a) and (d) Top and side views, (b) and (e) plane and three-dimensional charge density differences, (c) and (f) projected band structures of vdW PtS_2–STaTe and PtS_2–TeTaS heterostructures, respectively. The red dashed lines in (a) and (d) represent the unit cell of heterostructures. In both (b) and (e), the isosurface of charge density differences is 1.8×10^{-4} e $Bohr^{-3}$, the yellow and cyan regions of three-dimensional charge density differences represent the electron accumulation and depletion, respectively. The orange and blue colors in band structures represent the contributions from PtS_2 and TaSTe, respectively.

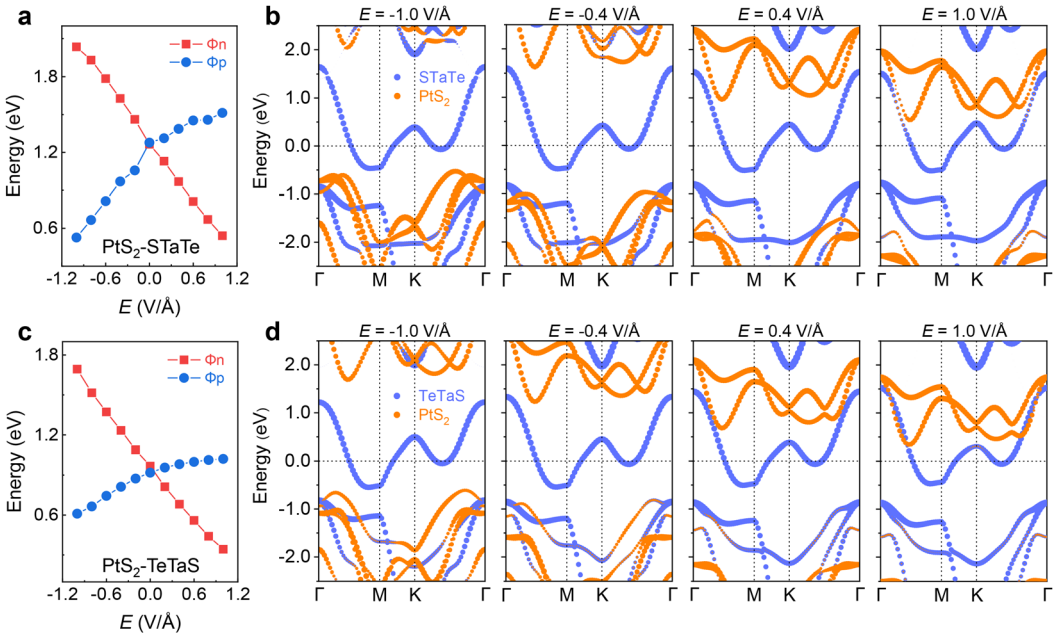

Fig. 3 Evolutions of SBH and the projected band structures under different external electric fields for (a) and (b) vdW PtS_2–STaTe, (c) and (d) vdW PtS_2–TeTaS heterostructures, respectively. Orange and blue colors in band structures represent the contributions from PtS_2 and TaSTe, respectively.

gradually decreases, while the n-type SBH increases, giving rise to a transition from n-type Schottky contact to the p-type Schottky contact. In experiments, although n-type or p-type conductivity has been observed in PtS_2-based field-effect transistors, achieving ambipolar conduction through transition metal contacts remains elusive.[33,34,39,40] Notably, in this work, both conductivity types have been realized in a single device, thus demonstrating the highly flexible tunability of conduction

characteristics of PtS_2-based field-effect transistors based on the external electric fields.

To elucidate the underlying mechanism, we systematically study the influence of the electric field on the band structures of the Schottky junction. As shown in Fig. 3b, when a positive external electric field set in the VASP code is applied (corresponding to the negative direction in common definition), the electric field points from PtS_2 to STaTe, thereby lowering the electrostatic potential of PtS_2 and shifting the conduction band minimum of PtS_2 close to the Fermi level, which is consistent with the mechanism proposed by a previous study.[37] This results in a reduction of the n-type SBH while increasing the p-type SBH. Conversely, when a negative external electric field is applied, the electric field points from STaTe to PtS_2, raising the electrostatic potential of PtS_2 and shifting the conduction band minimum away from the Fermi level. Consequently, the n-type SBH increases, while the p-type SBH decreases, leading to a conversion between p-type and n-type Schottky contacts near the zero electric field. Similarly, the PtS_2–TeTaS Schottky junction exhibits analogous electric-field-dependent SBH evolution but with a lower SBH compared to PtS_2–STaTe (Fig. 3c and d). Our findings demonstrate that electric fields possess the capability to effectively modulate the SBH, while the asymmetric contacts of the Janus metal electrode yield distinct modulation results at the M–S interface. We further evaluated the electric field response capability of PtS_2–STaTe and PtS_2–TeTaS Schottky junctions. According to previous reports, the slope of the Schottky barrier in conjunction with the electric field can be effectively used to describe the sensitivity of SBH to electric field modulation.[14,37] Fig. S4 reveals that the evolution of SBHs under different electric fields for the PtS_2–STaTe heterostructure exhibits a steeper slope than that for the PtS_2–TeTaS heterostructure, which indicates that the PtS_2–STaTe interface is more sensitive to external electric fields, suggesting a weaker electrostatic shielding effect.

Analogous to the effect of external electric fields, the external vertical strains will change the interlayer distance and interfacial coupling, providing a promising approach to tune the M–S interlayer characteristics and enable the reversible switching of contact types. The strain is denoted as $\Delta d = d - d_0$, where d_0 and d represent the interlayer distance without and with the applied strain, respectively. Notably, for the PtS_2–STaTe Schottky junction, tension strain ($\Delta d > 0$) induces a decrease in Φ_n and an increase in Φ_p, facilitating the n-type Schottky contact (Fig. 4a). In contrast, compression strain ($\Delta d < 0$) results in a decrease in Φ_p and an increase in Φ_n, forming the p-type Schottky contact. Consequently, the SBHs and reversible switching contact types of PtS_2–STaTe Schottky junction can be modified through the vertical strains. As shown in Fig. 4b, as the interlayer distance decreases, the projected band structures of the PtS_2 layer move upward, resulting in a reduction of Φ_p and an increase of Φ_n. In contrast, when gradually increasing the interlayer distance, the projected band structures of PtS_2 shift downwards, which results in a decreasing n-type Schottky barrier and an increasing p-type Schottky barrier. For the PtS_2–TeTaS Schottky junction, similar behaviors are observed (Fig. 4c and d), characterized by the reversible transitions from n-type to p-type contacts when changing the tension strain to compression strain, which is also induced by band structure shifts of PtS_2. It is noteworthy that as Δd is reduced to −1.0 Å, Φ_p of the PtS_2–TeTaS Schottky junction is below zero, enabling the reversible switching from the Schottky contact to ohmic contact, further

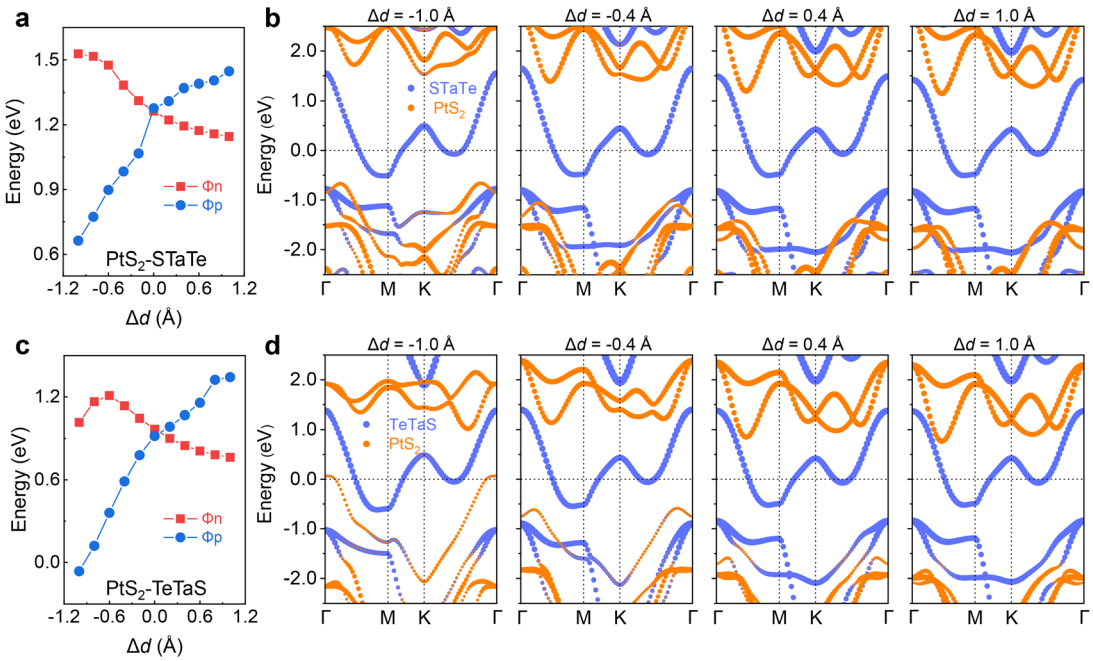

Fig. 4 Evolutions of SBH and the projected band structures under different compression and tension strains for (a) and (b) vdW PtS_2–STaTe, (c) and (d) vdW PtS_2–TeTaS heterostructures, respectively. Orange and blue colors in band structures represent the contributions from PtS_2 and TaSTe, respectively.

demonstrating the tunability of types and barriers of interfacial contacts.

As shown in Fig. 4a and c, both PtS_2–STaTe and PtS_2–TeTaS Schottky junctions exhibit faster SBH modulation under compression strain than tension strain. To clarify this phenomenon, we further analyzed the effect of interlayer distance on the interfacial charge distributions (Fig. S5 and S6). For comparison purposes, the *z*-coordinates in the figures are manually aligned with the *z*-coordinate of Janus TaSTe. The charge density difference is defined as: $\Delta\rho = \rho - \rho_{PtS_2} - \rho_{TaSTe}$, where ρ, ρ_{PtS_2}, and ρ_{TaSTe} represent the charge density of the heterostructure, PtS_2 and TaSTe, respectively. The charge density difference shown in Fig. S5 reveals electron accumulation at the center of the PtS_2–STaTe heterostructure interface, whereas it shows electron depletion at each side of the heterostructure interface. The application of progressive compressive strain gradually strengthens the coulomb repulsion, thereby decreasing central electron accumulation and enhancing peripheral depletion. At the critical strain ($\Delta d = -0.8$ Å), interfacial electron accumulation is mostly suppressed. Conversely, tension strain progressively attenuates both electron accumulation and depletion at the heterostructure due to weakened interfacial interactions, contrasting with the cases of compression strain. This expedited charge redistribution induced by compression strain enhances the tunability of SBH, with similar behaviors observed in the PtS_2–TeTaS junction (Fig. S6).

To reveal the mechanism of the strain-induced transition of SBH, we systematically investigated the effect of strain on the interfacial polarization caused by the asymmetric charge distributions in PtS_2–TaSTe heterostructures. For original STaTe and TeTaS monolayers, their polarizations have equal magnitudes but opposite orientations: 0.19 Debye per u.c. and −0.19 Debye per u.c., respectively. Fig. 5a shows that the total polarization of the PtS_2–STaTe heterostructure is 0.18 Debye per u.c. Since the total polarization of the heterostructure equals the sum of the intrinsic polarization of TaSTe and the interfacial polarization generated at the heterostructure interface, the interfacial polarization resulting from asymmetric electron redistribution is −0.01 Debye per u.c. with the direction opposed to that of the STaTe monolayer. Under compression strain, the interfacial polarization initially diminishes, undergoes a sign reversal from negative to positive at $\Delta d = -0.4$ Å, and subsequently increases gradually, ultimately leading to continuous strengthening of the overall polarization intensity in the heterostructure. Conversely, under the tension strain, the increasing interlayer distance weakens interfacial interactions and the corresponding polarization orientation remains opposite to that of STaTe, ultimately leading to a continuous reduction in the overall polarization of the heterostructure.

For the PtS_2–TeTaS Schottky junction (Fig. 5b), the interface exhibits opposite polarization relative to the TeTaS monolayer and the total polarization of the heterostructure is −0.1 Debye per u.c. Under the compression strain, the interfacial polarization magnitude increases and maintains its opposite polarization orientation to that of TeTaS, thereby reducing the total polarization of the heterostructure. Under the tension strain, however, the gradually weakened interfacial polarization with an opposite direction conversely enhances total polarization of the heterostructure. Fig. 5c, d and Fig. S7 illustrate a linear relationship between the strength of interfacial polarization and SBHs for both PtS_2–STaTe and PtS_2–TeTaS Schottky

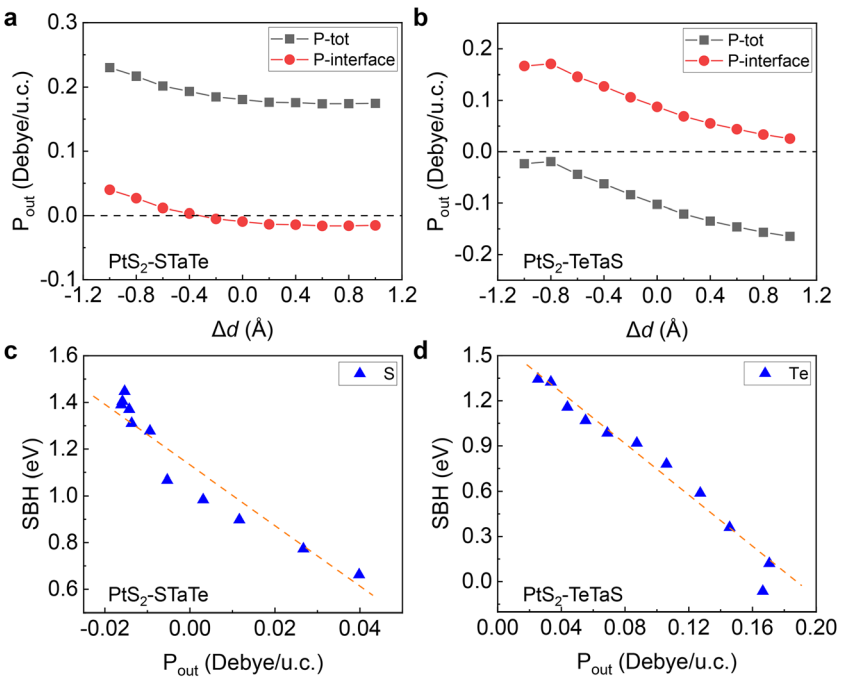

Fig. 5 (a) and (b) Out-of-plane total polarizations and interfacial polarizations *versus* different compression and tension strains, (c) and (d) evolutions of the p-type SBH *versus* the out-of-plane interfacial polarizations for vdW PtS_2–STaTe and PtS_2–TeTaS heterostructures, respectively. The dashed lines in (c) and (d) indicate the variation trend of SBH *versus* interfacial polarization.

junctions, which demonstrates strong dependency of the SBHs on the polarization induced by interfacial charge redistributions. Therefore, interfacial polarization strength is demonstrated as a critical factor for tuning the SBH at M–S contacts, and further modulations can be achieved by introducing elements with different electronegativities at the heterostructure interface.

To further study the underlying mechanism connecting interfacial charge redistribution and band alignment of heterostructures, we have calculated the charge transfer between TaSTe and PtS_2 in the PtS_2–TaSTe heterostructures. As shown in Fig. S8, when the compression strain is larger than 0.4, the strong interfacial interaction drives electrons to transfer from STaTe to PtS_2. According to the previous study,[37] this creates the built-in polarization electric field directed from STaTe to PtS_2, resulting in a spatial electrostatic potential gradient that rises the electrostatic potential of PtS_2. Consequently, the band edges of PtS_2 shift upward relative to the Fermi level, thereby increasing the n-type SBH. Conversely, when decreasing the compression strain, the weakened interlayer interaction leads to the electron transfer from PtS_2 to STaTe. This establishes a built-in polarization electric field from PtS_2 to STaTe, creating a potential gradient that lowers the electrostatic potential of PtS_2. As a result, the band edges of PtS_2 shift downward relative to the Fermi level, leading to a decrease in the n-type SBH. Similar mechanism can also be appropriate for the PtS_2–TeTaS heterostructure.

Due to the weak vdW interactions at the M–S interface, an interfacial tunneling barrier exists alongside the Schottky barrier, which serves as a critical factor for evaluating the carrier transport efficiency across the heterostructure interface. As shown in Fig. 6a and d, we calculated the average electrostatic potential perpendicular to the M–S contact interface for PtS_2–STaTe and PtS_2–TeTaS, where the height of the barrier, Φ_{TB}, and the width of the barrier, d_{TB}, are two key parameters for evaluating the tunnelling barriers. We find that compression strain reduces interface distance and enhances interfacial coupling, thereby decreasing both Φ_{TB} and d_{TB}. Conversely, tension strain increases interlayer spacing and weakens interfacial interaction, leading to an increase in both Φ_{TB} and d_{TB} at the interface. The carrier tunneling probability can be calculated as follows:[16,41,42]

$$T_B = \exp\left(-2 \times \frac{\sqrt{2m\Phi_{TB}}}{\hbar} \times d_{TB}\right) \quad (1)$$

where $\hbar$ is the reduced Planck's constant and m is the electron mass. Therefore, the tunneling probability exponentially decays with the root of Φ_{TB} and d_{TB}. Fig. 6b reveals that the tunneling probability increases sharply from 3.36% (Δd = 0 Å) to 67.37% (Δd = −1.0 Å), while under tension strain, the tunnelling probability decreases and eventually tends to 0. Therefore, employing the compression strain emerges as a potent strategy for augmenting interfacial transport in vdW M–S contacts.

In addition to tunnelling probability, tunnelling-specific resistivity is another key factor for evaluating the quality of M–S contacts. According to the Simmons tunneling injection model under the low-bias approximation, tunneling-specific

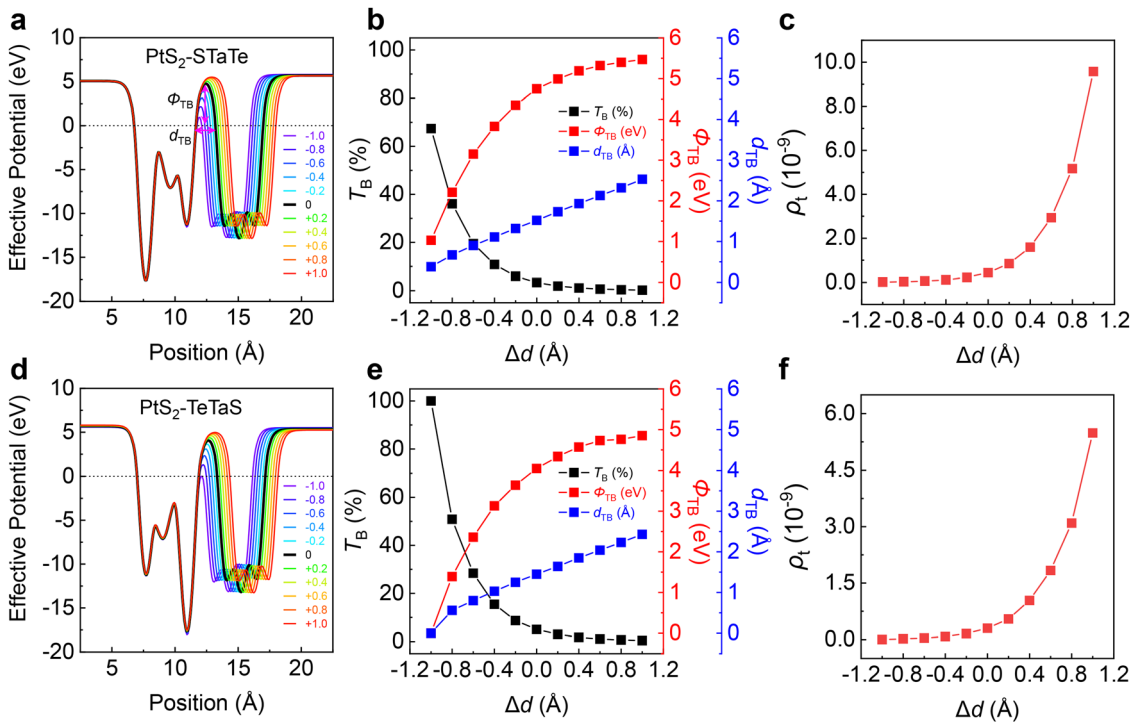

Fig. 6 (a) and (d) Out-of-plane effective potential, (b) and (e) tunneling probability T_B and tunneling barrier including barrier height Φ_{TB} and barrier width d_{TB}, (c) and (f) tunneling-specific resistivity for vdW PtS_2–STaTe and PtS_2–TeTaS heterostructures under different compression and tension strains, respectively.

resistivity can be calculated using the following equation:[6,43]

$$\rho_t \approx \frac{8\pi^2 d_{TB}{}^2}{3(2m\Phi_{TB})^{1/2}e^2}\exp\left[\frac{2d_{TB}(2m\Phi_{TB})^{1/2}}{}\right] \quad (2)$$

where e is the electron charge, and the tunneling-specific resistivity is proportional to Φ_{TB} and d_{TB}. Fig. 6c shows that the initial tunneling-specific resistivity is 4.33×10^{-10} Ω cm^2, which is an order of magnitude lower than that of the reported Bi–MoS_2 contact and metal–Mo(W)Si_2N_4 contacts.[6,43] Under compression strain, the tunneling-specific resistivity decreases from 4.33×10^{-10} Ω cm^2 to 1.18×10^{-11} Ω cm^2, whereas it elevates from 4.33×10^{-10} Ω cm^2 to 9.58×10^{-9} Ω cm^2 under tension strain. For the PtS_2–TeTaS Schottky interface (Fig. 6d–f), although strain-dependent trends of Φ_{TB} and d_{TB} are similar to those of the PtS_2–STaTe interface, their magnitudes remain relatively smaller. According to eqn (1) and (2), the PtS_2–TeTaS interface exhibits a higher tunneling probability, but a lower tunneling-specific resistivity than the PtS_2–STaTe interface, highlighting the tunable contact behaviors facilitated by the Janus metal.

Considering that the number of semiconductor layers modulates both the bandgap and Fermi level, it should exert significant modulating effects on the M–S contact. We have systematically investigated the layer dependent effects on M–S interfacial properties. Fig. S9a and c depict that the charge redistributions in 2L PtS_2 and Janus TaSTe contacts remain predominantly localized at the heterogeneous interface with minor charge transfer occurring between two PtS_2 layers, which resembles the case in monolayer Schottky junctions. However, different from monolayer Schottky junctions, both 2L PtS_2–STaTe and 2L PtS_2–TeTaS Schottky interfaces exhibit significantly reduced SBH with the transition to p-type characteristics (Fig. S9b and d). As shown in Fig. S10, under an external electric field, the transition behavior between p-type and n-type Schottky barriers occurs at both PtS_2–STaTe and PtS_2–TeTaS Schottky interfaces but primarily under a positive electric field of 0.4 and 0.1 V Å^{-1}, respectively. On the other hand, the transition from the p-type Schottky contact to ohmic contact emerges with SBH less than zero under a large negative electric field (>-0.6 V Å^{-1}), suggesting a prominent modulation compared to monolayers (Fig. S10a and c). More interestingly, PtS_2–STaTe and PtS_2–TeTaS Schottky interfaces display distinct modulation trends under the effect of strain (Fig. S11). For the PtS_2–STaTe interface, the p-type Schottky contact is maintained regardless of compression or tension strain. In contrast, the PtS_2-TeTaS Schottky interface exhibits conversion between p-type and n-type Schottky contacts under a tension strain of Δd = 0.3 Å. Moreover, under a compression strain of $\Delta d = -0.8$ Å, a transition from p-type to ohmic contact behavior is observed.

We further elucidated the underlying mechanism of the strain-induced transition of SBH. As shown in Fig. S12, similar to the cases in monolayer Schottky junctions, the polarization at the 2L PtS_2–STaTe and 2L PtS_2–TeTaS Schottky interfaces exhibits a gradual decreasing trend as the electric field transitions from negative to positive. Correspondingly, we find that the SBH is also inversely proportional to the interfacial polarization. Subsequently, we studied the corresponding interfacial tunnelling behavior (Fig. S13). Different from monolayer M–S contacts, bilayer PtS_2 and Janus TaSTe contacts exhibit both interfacial barriers and interlayer barriers (interface between two PtS_2 layers). Crucially, the interfacial barrier dominates with a larger barrier height and width than those of the interlayer barriers. Tunnelling barriers, tunnelling probabilities, and tunnelling-specific resistivity of 2L PtS_2–STaTe and 2L PtS_2–TeTaS Schottky interfaces follow the similar trends as those of monolayer cases, confirming that atomic interactions at the interfaces play the determining role in tuning the SBH. Additionally, layer-dependent effects on M–S contacts were also further investigated (Fig. S14 and S15). M–S contacts maintain the p-type Schottky contacts with decreasing SBH as PtS_2 layers increase. For PtS_2–STaTe, the p-type barrier is reduced to 0.06 eV in 4-layer PtS_2 systems, nearly forming an ohmic contact. Conversely, PtS_2–TeTaS still exhibits a 0.30 eV p-type barrier even in 4-layered PtS_2. Therefore, through dual interface engineering based on metallic Janus TaSTe, we achieved simultaneous modulation of SBH and implementation of asymmetric Schottky contacts within a single metallic electrode, which demonstrates significant potential applications in field-effect transistors.

The interface engineering strategy based on Janus metals is further envisioned in other metallic Janus systems. Specifically, we analyzed diverse M–S contacts by substituting the Ta element with various transition metal elements, including Hf, Zr, Ti, Nb, and Cr elements. It should be noted that this work mainly focuses on the modulation behaviors of Schottky contacts by using these extended systems, while structural stability considerations are beyond our research scope. Significantly, as shown in Fig. 7 and Table S4, our results demonstrate that when substituting Ta with these metallic elements, both S and Te interfaces-based heterostructures exhibit an obviously tunable SBH. Taking PtS_2 and HfSTe systems as an example, the PtS_2–SHfTe interface demonstrates an n-type SBH of 0.56 eV, while the PtS_2–TeHfS interface displays an n-type SBH of 0.39 eV. To further quantitatively describe the Fermi-level pinning effect, we calculated the Fermi-level pinning factor using the equation: $S = |d\Phi_{SB}/dW_{metal}|$, where W_{metal} is the work function of metal, S = 1 represents the Schottky–Mott limit without Fermi-level pinning, while S = 0 means strong Fermi-level pinning. As shown in Fig. 7b and d, the Fermi-level pinning factors for n-type Schottky and p-type Schottky contacts were 0.68 and 0.64, respectively, which significantly exceed the values for the conventional M–S contacts, indicating the superior tunability of SBHs in PtS_2 and Janus metal contacts.

We further investigated whether modifying the non-metallic element at the termination of the Janus metal can modulate the SBHs, as illustrated in Fig. 8a. By replacing the S element with the P element, we found that the SBH of the PtS_2–PTaTe system is 0.84 eV, while the SBH of the PtS_2–TeTeP system is 0.29 eV, which demonstrates significant tunability of SBH. Moreover, we also investigated the tunability of M–S contacts between Janus metals and other semiconductors such as MoS_2. As shown in Fig. 8b, the MoS_2–STaTe system shows the p-type SBH of 0.90 eV, whereas the MoS_2–TeTaS system exhibits the n-type

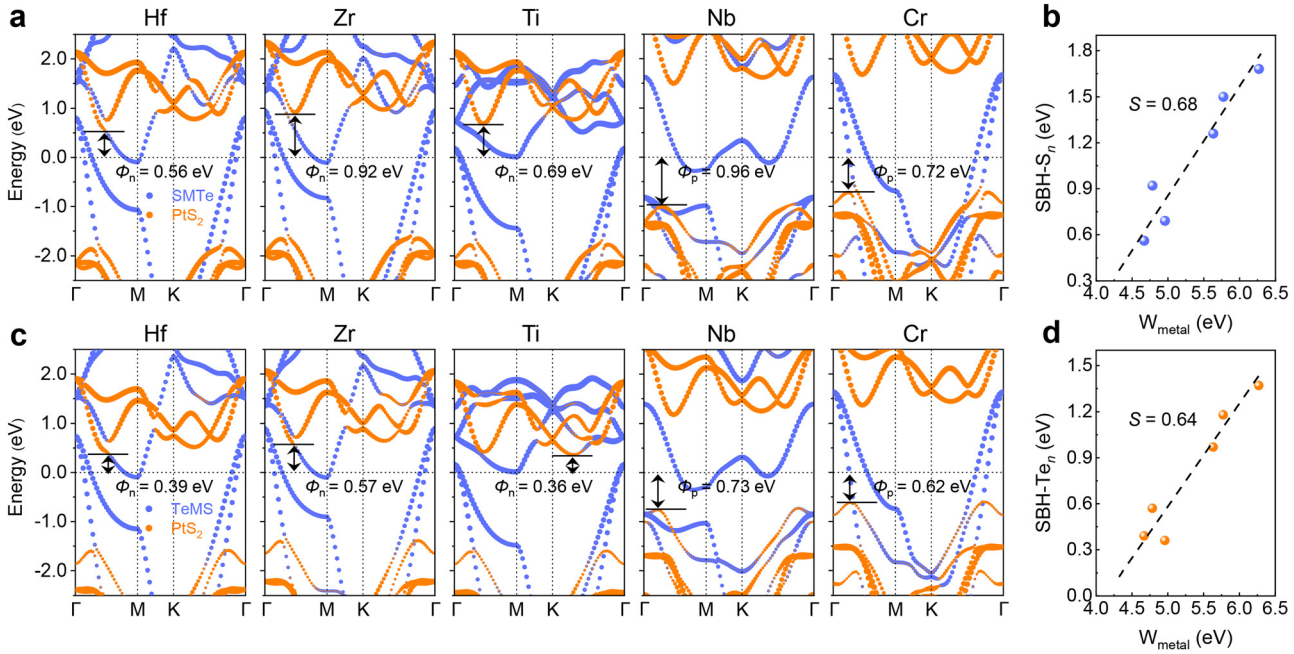

Fig. 7 The projected band structures and Fermi-level pinning factors for vdW (a) and (b) PtS_2–SMTe, (c) and (d) PtS_2–TeMS heterostructures, respectively. Here, M represents the transition metal elements including Hf, Zr, Ti, Nb, and Cr. Orange and blue colors in band structures represent the contributions from PtS_2 and MSTe, respectively.

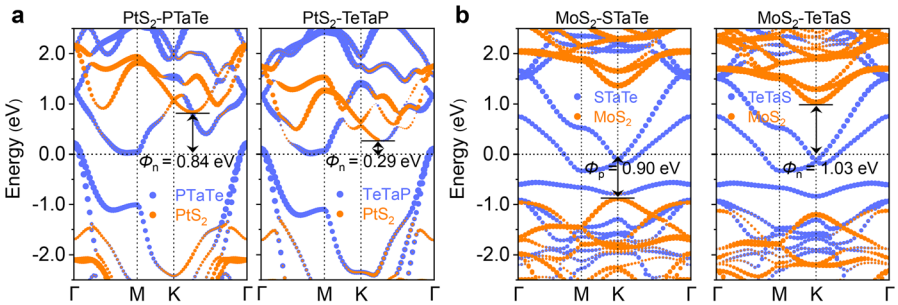

Fig. 8 (a) The projected band structures for vdW PtS_2–PTaTe (left part) and PtS_2–TeTaP (right part) heterostructures, respectively. Orange and blue colors in band structures represent the contributions from PtS_2 and TaPTe, respectively. (b) The projected band structures for vdW MoS_2–STaTe (left part) and MoS_2–TeTaS (right part) heterostructures, respectively. Orange and blue colors in band structures represent the contributions from MoS_2 and TaSTe, respectively.

SBH of 1.03 eV, which also highlights the tunability of SBHs. In general, our results demonstrate that on one hand, varying transition metal elements in Janus metals yields distinct work functions, resulting in modulated SBH across different metal systems; on the other hand, divergent electronegativities of nonmetallic elements at the termination of Janus metals result in distinct M–S interfacial interactions, facilitating tunable Schottky contacts. The results not only break through the limitation of the dimension of singular work function in tuning the SBHs but also demonstrate the universality of our research for achieving the tunable SBHs based on the Janus metals. Finally, we also compared our proposed SBH engineering strategy with the established methods including work function engineering or interface dipole modification. As shown in Table S5, although all these engineering methods show a wide range of tunability, stable issues and implementation complexity, various electrodes need to be applied for achieving work function engineering, while the interface dipole modification is only valid for the out-of-plane polar semiconductors, which severely limits the practical applications. In contrast, we present a more practical alternative, achieving effective Schottky barrier modulation with singular electrode and unrestricted semiconductor types. More importantly, we here mainly focus on the new engineering strategy based on the Janus metal, which provides a new perspective for manipulating the SBHs in metal–semiconductor contacts.

Conclusions

In summary, we have shown that the metallic Janus TaSTe with novel geometric and electronic structures provides an innovative way to achieve the tunable SBH in metal and

semiconductor contacts. Our first-principles calculations reveal the out-of-plane polarization nature of metallic Janus TaSTe due to the out-of-plane broken mirror symmetry and asymmetric charge density distributions arising from the different electronegativities of S and Te elements. Effective modulation of the SBH can be achieved through the conversion of the S/Te interface with PtS_2. In addition, both the electronic properties and interfacial characteristics of the PtS_2–STaTe and PtS_2–TeTaS heterostructures can be effectively tuned by the external electric fields and strain, leading to the interconversion between n-type and p-type Schottky contacts. Furthermore, we have investigated the different contacts in different Janus metals and semiconductors and find that the SBH can also be effectively regulated, demonstrating the universality of our results. Our findings go beyond the limitation of singular work function and provide insight into the interface properties of Janus metal and semiconductor contacts, which shows great potential for applications in high-performance electronic devices.

Author contributions

Shaojuan Li and Liujian Qi conceived the original concept and supervised the project. Liujian Qi and Yanze Feng performed the DFT calculations and theoretical analysis. Y. F., L. Q., Y. D., N. Z., Y. Z., Z. S., D. L., and S. L. analyzed the data and co-wrote the paper. All authors discussed the results and commented on the manuscript.

Conflicts of interest

There are no conflicts to declare.

Data availability

The data supporting this article have been included as part of the supplementary information (SI). Supplementary information: computational data including structural models, binding energies, electronic band structures, charge density differences, and the evolution of SBHs under different strains, electric fields, and layer numbers. See DOI: **https://doi.org/10.1039/d5mh01553g**.

Acknowledgements

We acknowledge the financial support from the National Natural Science Foundation of China (62204240, 62334010, 62121005, and 62525407), the National Key Research and Development Program (2021YFA0717600), the Natural Science Foundation of Jilin Province (20250101001JJ, 20240602062RC), the Changchun Key Research and Development Program (23GZZ11), and the ''Shu Guang'' Talent Program of Changchun Institute of Optics, Fine Mechanics and Physics, Chinese Academy of Sciences.

References

1 Y.-L. Hong, Z. Liu, L. Wang, T. Zhou, W. Ma, C. Xu, S. Feng, L. Chen, M.-L. Chen, D.-M. Sun, X.-Q. Chen, H.-M. Cheng and W. Ren, *Science*, 2020, **369**, 670–674.
2 X. Yang, J. Li, R. Song, B. Zhao, J. Tang, L. Kong, H. Huang, Z. Zhang, L. Liao, Y. Liu, X. Duan and X. Duan, *Nat. Nanotechnol.*, 2023, **18**, 471–478.
3 X. Yu, P. Yu, D. Wu, B. Singh, Q. Zeng, H. Lin, W. Zhou, J. Lin, K. Suenaga, Z. Liu and Q. J. Wang, *Nat. Commun.*, 2018, **9**, 1545.
4 C. Wang, L. You, D. Cobden and J. Wang, *Nat. Mater.*, 2023, **22**, 542–552.
5 Y. Feng, R. Chen, J. He, L. Qi, Y. Zhang, T. Sun, X. Zhu, W. Liu, W. Ma, W. Shen, C. Hu, X. Sun, D. Li, R. Zhang, P. Li and S. Li, *Nat. Commun.*, 2023, **14**, 6739.
6 P.-C. Shen, C. Su, Y. Lin, A.-S. Chou, C.-C. Cheng, J.-H. Park, M.-H. Chiu, A.-Y. Lu, H.-L. Tang, M. M. Tavakoli, G. Pitner, X. Ji, Z. Cai, N. Mao, J. Wang, V. Tung, J. Li, J. Bokor, A. Zettl, C.-I. Wu, T. Palacios, L.-J. Li and J. Kong, *Nature*, 2021, **593**, 211–217.
7 Y. Wang, J. C. Kim, Y. Li, K. Y. Ma, S. Hong, M. Kim, H. S. Shin, H. Y. Jeong and M. Chhowalla, *Nature*, 2022, **610**, 61–66.
8 C. Kim, I. Moon, D. Lee, M. S. Choi, F. Ahmed, S. Nam, Y. Cho, H.-J. Shin, S. Park and W. J. Yoo, *ACS Nano*, 2017, **11**, 1588–1596.
9 Y. Liu, J. Guo, E. Zhu, L. Liao, S.-J. Lee, M. Ding, I. Shakir, V. Gambin, Y. Huang and X. Duan, *Nature*, 2018, **557**, 696–700.
10 W. Li, X. Gong, Z. Yu, L. Ma, W. Sun, S. Gao, Ç. Köroğlu, W. Wang, L. Liu, T. Li, H. Ning, D. Fan, Y. Xu, X. Tu, T. Xu, L. Sun, W. Wang, J. Lu, Z. Ni, J. Li, X. Duan, P. Wang, Y. Nie, H. Qiu, Y. Shi, E. Pop, J. Wang and X. Wang, *Nature*, 2023, **613**, 274–279.
11 X. Li, Y. Wei, Z. Wang, Y. Kong, Y. Su, G. Lu, Z. Mei, Y. Su, G. Zhang, J. Xiao, L. Liang, J. Li, Q. Li, J. Zhang, S. Fan and Y. Zhang, *Nat. Commun.*, 2023, **14**, 111.
12 S. Song, A. Yoon, S. Jang, J. Lynch, J. Yang, J. Han, M. Choe, Y. H. Jin, C. Y. Chen, Y. Cheon, J. Kwak, C. Jeong, H. Cheong, D. Jariwala, Z. Lee and S.-Y. Kwon, *Nat. Commun.*, 2023, **14**, 4747.
13 Y. Li, L. Su, Y. Lu, Q. Luo, P. Liang, H. Shu and X. Chen, *InfoMat*, 2023, **5**, e12407.
14 T. Shen, J. Liu, X. Liu, P. Cheng, J.-C. Ren, S. Li and W. Liu, *Adv. Funct. Mater.*, 2022, **32**, 2207018.
15 Y. Liu, P. Stradins and S.-H. Wei, *Sci. Adv.*, 2016, **2**, e1600069.
16 X. Zhang, L. Feng, S. Zhong, Y. Ye, H. Pan, P. Liu, X. Zheng, H. Li, M. Qu and X. Wang, *Sci. China Mater.*, 2023, **66**, 811–818.
17 N. T. T. Binh, C. Q. Nguyen, T. V. Vu and C. V. Nguyen, *J. Phys. Chem. Lett.*, 2021, **12**, 3934–3940.
18 Z. H. Li, J. N. Han, S. G. Cao and Z. H. Zhang, *Appl. Surf. Sci.*, 2023, **614**, 156095.
19 Y. Cao, Z. Wang, S. Y. Park, Y. Yuan, X. Liu, S. M. Nikitin, H. Akamatsu, M. Kareev, S. Middey, D. Meyers, P. Thompson, P. J. Ryan, P. Shafer, A. N'Diaye, E. Arenholz,

V. Gopalan, Y. Zhu, K. M. Rabe and J. Chakhalian, *Nat. Commun.*, 2018, **9**, 1547.
20 Y.-W. Fang and H. Chen, *Commun. Mater.*, 2020, **1**, 1.
21 Y. Yin, Q. Gong, M. Yi and W. Guo, *Mater. Horiz.*, 2023, **10**, 5177–5184.
22 T. Xu, J. Zhang, Y. Zhu, J. Wang, T. Shimada, T. Kitamura and T.-Y. Zhang, *Nanoscale Horiz.*, 2020, **5**, 1400–1406.
23 F. Li, W. Wei, P. Zhao, B. Huang and Y. Dai, *J. Phys. Chem. Lett.*, 2017, **8**, 5959–5965.
24 R. Ku, L. Yan, J.-G. Si, S. Zhu, B.-T. Wang, Y. Wei, K. Pang, W. Li and L. Zhou, *Phys. Rev. B*, 2023, **107**, 064508.
25 G. Kresse and D. Joubert, *Phys. Rev. B:Condens. Matter Mater. Phys.*, 1999, **59**, 1758–1775.
26 P. E. Blöchl, *Phys. Rev. B:Condens. Matter Mater. Phys.*, 1994, **50**, 17953–17979.
27 J. P. Perdew, K. Burke and M. Ernzerhof, *Phys. Rev. Lett.*, 1996, **77**, 3865–3868.
28 S. Grimme, J. Antony, S. Ehrlich and H. Krieg, *J. Chem. Phys.*, 2010, **132**, 154104.
29 J. Heyd, J. E. Peralta, G. E. Scuseria and R. L. Martin, *J. Chem. Phys.*, 2005, **123**, 174101.
30 W. Shi and Z. Wang, *J. Phys.: Condens. Matter.*, 2018, **30**, 215301.
31 J. Zhang, S. Jia, I. Kholmanov, L. Dong, D. Er, W. Chen, H. Guo, Z. Jin, V. B. Shenoy, L. Shi and J. Lou, *ACS Nano*, 2017, **11**, 8192–8198.
32 Y. Li, D. Legut, X. Liu, C. Lin, X. Feng, Z. Li and Q. Zhang, *J. Phys. Chem. C*, 2022, **126**, 8817–8825.
33 Z. Wang, P. Wang, F. Wang, J. Ye, T. He, F. Wu, M. Peng, P. Wu, Y. Chen, F. Zhong, R. Xie, Z. Cui, L. Shen, Q. Zhang, L. Gu, M. Luo, Y. Wang, H. Chen, P. Zhou, A. Pan, X. Zhou, L. Zhang and W. Hu, *Adv. Funct. Mater.*, 2020, **30**, 1907945.
34 L. Li, W. Wang, Y. Chai, H. Li, M. Tian and T. Zhai, *Adv. Funct. Mater.*, 2017, **27**, 1701011.
35 P. Manchanda, A. Enders, D. J. Sellmyer and R. Skomski, *Phys. Rev. B*, 2016, **94**, 104426.
36 Y. Zhang, Y. Shen, L. Lv, M. Zhou, X. Yang, X. Meng, N. Zhang, K. Wang, B. Zhang and Z. Zhou, *Phys. Rev. Appl.*, 2023, **20**, 044066.
37 C. V. Nguyen, P. T. Truong, H. V. Phuc, C. Q. Nguyen, N. T. Hiep and N. N. Hieu, *Nano Lett.*, 2025, **25**, 10673–10679.
38 X. Wei, M. Zhang, X. Zhang, Y. Lin, Z. Jiang and A. Du, *J. Phys. Chem. Lett.*, 2024, **15**, 3871–3883.
39 J. Lu, X. Zhang, G. Su, W. Yang, K. Han, X. Yu, Y. Wan, X. Wang and P. Yang, *Mater. Today Phys.*, 2021, **18**, 100376.
40 D. Zhao, S. Xie, Y. Wang, H. Zhu, L. Chen, Q. Sun and D. W. Zhang, *AIP Adv.*, 2019, **9**, 025225.
41 L. Qi, M. Che, M. Liu, B. Wang, N. Zhang, Y. Zou, X. Sun, Z. Shi, D. Li and S. Li, *Nanoscale*, 2023, **15**, 13252–13261.
42 Z. Xu, M. Chen and S. F. Liu, *J. Phys. Chem. Lett.*, 2021, **12**, 1718–1725.
43 Q. Wang, L. Cao, S.-J. Liang, W. Wu, G. Wang, C. H. Lee, W. L. Ong, H. Y. Yang, L. K. Ang, S. A. Yang and Y. S. Ang, *npj 2D Mater. Appl.*, 2021, **5**, 71.

